Submitted to ADVANCED MATERIALS
DOI: 10.1002/adma. ((please add manuscript number))
Article type: Communication

Synthesis of Co-doped MoS_2 monolayer with enhanced valley splitting

Jiadong Zhou[1+], Junhao Lin[2,3+], Hunter Sims[4, 5+], Chongyun Jiang[6,7+], Chunxiao Cong[6,8], John A. Brehm[4,5], Zhaowei Zhang[6], Lin Niu[1], Yu Chen[6], Yao Zhou[6], Yanlong Wang[6], Fucai Liu[1], Chao Zhu[1], Ting Yu[6], Kazu Suenaga[2], Rohan Mishra[9], Sokrates T. Pantelides[4,5,14], Zhen-Gang Zhu[10,11], Weibo Gao[6*], Zheng Liu[1,12,13*], and Wu Zhou[11,14*]*

Dr. J. Zhou, Dr. L. Niu, Dr. F. Liu, Mr. C. Zhu, Prof. Z. Liu
School of Materials Science and Engineering, Nanyang Technological University, Singapore 639798, Singapore.
Z.L. (email: z.liu@ntu.edu.sg)

Dr. J. Lin
National Institute of Advanced Industrial Science and Technology (AIST), Tsukuba 305-8565, Japan
Department of Physics, Southern University of Science and Technology, Shenzhen 518055, China

Prof K Suenaga
National Institute of Advanced Industrial Science and Technology (AIST), Tsukuba 305-8565, Japan

Dr. H. Sims, Dr. J. Brehm, Prof. S. Pantelides
Department of Physics and Astronomy, Vanderbilt University, Nashville, TN 37235, USA
Materials Science and Technology Division, Oak Ridge National Lab, Oak Ridge Tennessee 37831, USA

Dr. C. Jiang
Division of Physics and Applied Physics, School of Physical and Mathematical Sciences, Nanyang Technological University, Singapore 637371, Singapore
College of electronic information and optical engineering, Nankai University, Tianjin 300350, China

Dr. C. Cong
Division of Physics and Applied Physics, School of Physical and Mathematical Sciences, Nanyang Technological University, Singapore 637371, Singapore
State Key Laboratory of ASIC & System, School of Information Science and Technology, Fudan University, Shanghai 200433, P.R. China

Mr. Z. Zhang, Dr. Y. Chen, Dr. Y. Zhou, Dr. Y. Wang, Prof. T. Yu, Prof. W. Gao
Division of Physics and Applied Physics, School of Physical and Mathematical Sciences, Nanyang Technological University, Singapore 637371, Singapore
W.G. (email: wbgao@ntu.edu.sg)

Dr. R. Mishra

Department of Mechanical Engineering and Materials Science and Institute of Materials Science and Engineering, Washington University in St. Louis, St. Louis, Missouri 63130, USA

Prof. Z. Zhu
School of Electronic, Electrical and Communication Engineering, University of Chinese Academy of Science, Beijing 100049, China
CAS Center for Excellence in Topological Quantum Computation, University of Chinese Academy of Sciences, Beijing 100049, China
Z.Z. (email: zgzhu@ucas.ac.cn)

Prof. W. Zhou
CAS Center for Excellence in Topological Quantum Computation, University of Chinese Academy of Sciences, Beijing 100049, China
School of Physical Sciences and CAS Key Laboratory of Vacuum Sciences, University of Chinese Academy of Sciences, Beijing 100049, China
W.Z. (email: wuzhou@ucas.ac.cn)

Prof. Z. Liu
Centre for Micro-/Nano-electronics (NOVITAS), School of Electrical & Electronic Engineering, Nanyang Technological University, 50 Nanyang Avenue, Singapore 639798, Singapore

CINTRA CNRS/NTU/THALES, UMI 3288, Research Techno Plaza, 50 Nanyang Drive, Border X Block, Level 6, Singapore 637553, Singapore

Keywords: MoS_2, chemical vapor deposition, Co-doped, valley splitting, two-dimensional materials

Monolayer transition metal dichalcogenides (TMDCs) with broken inversion symmetry and direct band-gap offer the possibility to control their valley polarization for memory, logic and quantum devices applications[1-3]. Valley Zeeman splitting has been experimentally observed in pristine MX_2 (M=W or Mo; X=S, Se or Te) monolayers[4-13]; however, the achievable valley splitting and Landé g-factor in these pristine monolayers are relatively small. Theoretical studies predicted that a giant and tunable valley splitting can be obtained in monolayer $MoTe_2$ on a ferromagnetic EuO substrate due to the interfacial magnetic exchange field[14], which has recently been confirmed experimentally using monolayer WSe_2 on ferromagnetic EuS and CrI_3 substrates[15, 16]. In principle, internal magnetic moments induced by magnetic dopants in TMDC monolayers should also be able to engineer the valley splitting.

Theoretical studies have shown that local magnetism can be introduced in semiconducting MoS_2 via substitutional doping with magnetic elements, such as V, Cr, Mn, Fe, Co, or Ni[17-20]. The changes in the electronic and magnetic structures upon doping can subsequently affect the valley pseudospin. However, incorporating these magnetic dopants into monolayer MoS_2 lattice in a controllable manner remains challenging[21-23] and has hindered the systematic study of their influence on the valley pseudospin. Controlled synthesis of monolayer MoS_2 doped with specific magnetic elements is a desirable first step in order to explore the manipulation of valley pseudospin via internal magnetic moments.

In this work, we demonstrate the successful incorporation of a magnetic element（Co）into MoS_2 monolayers at various concentrations via chemical vapor deposition (CVD). The atomic configurations and chemical identities of the Co dopants were analyzed via annular dark-field (ADF) imaging and electron energy loss spectroscopy (EELS) at the single-atom level on an aberration-corrected low-voltage scanning transmission electron microscope (STEM). Both single dopants and tri-dopant triangular clusters were observed in Co-doped MoS_2. The presence of the tri-dopant clusters gives rise to enhanced valley Zeeman splitting in the Co-doped monolayer MoS_2, with values a few times larger than those for pristine TMDCs. More importantly, the magnitude of the valley Zeeman splitting can be tuned via controlling the concentration of Co dopants. Density functional theory (DFT) calculations confirm that the thermodynamic stability of Co dopants is enhanced by the formation of these triangular Co clusters surrounding a central sulfur vacancy. Further, these calculations reveal ferromagnetic coupling within the tri-dopant clusters, leading to an internal magnetic field in the Co-doped semiconducting MoS_2 monolayers. Finally, at doping levels of a few percent, it is shown that the internal magnetic field plays an essential role in the giant enhanced valley Zeeman splitting.

The overlapping of the dopant and carrier wave functions is the microscopic mechanism that underlies this observation.

The growth setup for doped MoS_2 monolayers is shown in Figure S1, and detailed information on the synthesis can be found in the Methods section. **Figure 1**a shows the optical image of a Co-doped MoS_2 monolayer sample. Most of the doped MoS_2 monolayer domains show the characteristic triangular shape frequently observed in CVD grown MoS_2, an indication of their high crystallinity. The optical image of MoS_2 on a large wafer is shown in Figure S2. The Co-doped MoS_2 with different dopant concentrations can be achieved by controlling the mole ratio of the precursors, as presented in Methods. The averaged doping concentration of the magnetic elements was analyzed via X-ray photoelectron spectroscopy (XPS) combined with STEM results. The peak positions of Co*2p* in the XPS spectra as shown in Figure S3 demonstrate the formation of chemical bonding between the dopant atoms and sulfur in the MoS_2 lattice, which is different from the CoMoS phase (see details in Figure S3). Atomic force microscopy (AFM) analysis confirms that the as-synthesized Co-doped MoS_2 domain is indeed monolayer, as shown in Figure S4. The Raman spectra of the Co-doped MoS_2 and pristine MoS_2 monolayers are shown in **Figure 1**b. All the doped samples display the characteristic A_g mode around ~ 401 cm^{-1} and the E_g mode around ~ 381 cm^{-1} in the Raman spectra, indicating that the Co-doped MoS_2 preserves similar lattice feature as the pristine MoS_2 crystals. Photoluminescence (PL) spectra in **Figure 1**c confirm the monolayer feature of the doped-MoS_2 samples. The corresponding Raman and PL mapping are shown in Figure S2, demonstrating the uniformity of Co-doped MoS_2.

We used atomic-resolution STEM-ADF imaging and EELS analysis to confirm the incorporation of magnetic dopants into the MoS_2 lattice and simultaneously identify their local atomic configurations. Theoretical studies have found that the magnetic elements can substitute Mo atoms in the MoS_2 lattice[20, 24], forming a single substitutional defect. **Figure 1**d shows the

STEM images of Co dopants in MoS_2 lattice. The Mo (brighter) atoms and S (dimmer) column can be clearly distinguished in the MoS_2 lattice, owing to the atomic number (Z) contrast in the STEM images. Due to the smaller atomic number of Co, they show similar contrast levels to that of the di-sulfur columns and lower than that of the Mo atoms in the STEM-ADF images. In other words, the dimmer contrast at the Mo sites is most likely arising from Co dopants. However, note that under sulfur-rich CVD growth conditions, di-sulfur (S_2) can occupy Mo sites forming anti-site defects[25], which generate similar STEM-ADF image contrast as observed here. In order to unambiguously confirm the incorporation of the magnetic dopants into the MoS_2 lattice, we further used atomic-scale STEM-EELS analysis to pinpoint the chemical identities of the low-contrast metal sites. EELS spectra acquired from the individual metal sites (**Figure 1**e) clearly show the characteristic $L_{2,3}$ edges of the Co dopants, confirming the formation of substitutional magnetic dopants into the MoS_2 lattice. Based on the STEM-ADF images, we found two distinct configurations of Co dopants in the MoS_2 lattice, namely the isolated single dopants and the tri-dopant clusters with a central S vacancy (V_S). Simulated STEM-ADF images along with the corresponding atomic structural models for the two types of dopant configurations are shown next to the experimental images, showing an excellent agreement.

To further validate the tunability of the Co dopant concentration in MoS_2 monolayer, we statistically examined the Co concentration in Co-doped MoS_2 monolayers with different designed dopant concentration. We sampled each flake in random regions and mapped out the Co dopants by their lower intensity, part of which were verified by corresponding single atom EELS measurements. **Figure 1**f shows representative 10nm×10nm regions of three Co-doped MoS_2 monolayers with different Co concentration. The Co concentration is estimated by atom counting of the Co dopants, which shows an average concentration of 0.9% ± 0.3%, 2.1% ± 0.5% and 6.6% ± 0.7% (from left to right), demonstrating the flexible tunability of Co dopant

concentration in MoS_2 lattice using our CVD method. The relative population ratio of the isolated single dopants (highlighted by light blue) and tri-dopant clusters with a central S vacancy (highlighted by green) are also provided in **Figure 1**f. It was found that at low doping concentration (**Figure 1**f left), Co atoms have almost equal probability to form either dopant configurations, while the tri-dopant cluster with a central S vacancy becomes the dominant configuration as the average Co concentration increases, suggesting that the excessive Co atoms tend to aggregate when substituting the metal sites in the MoS_2 lattice at high concentration.

DFT calculations on the formation and binding energies of the two types of Co dopant configurations further support the experimental observations. We find that it is energetically favorable for transition-metal impurities substituting Mo to form three-atom complexes with a central S vacancy, with a formation energy of 0.2 eV for a three-dopant cluster as compared to 2 eV for an isolated single dopant (Figure S5). Figure S5 also shows the formation energy of three-atom clusters (per dopant atom) without a central S vacancy for different elements. Even under S-rich growth conditions, the three-atom clusters of Co gain energy by losing the central S atom. The gain in energy upon the formation of a three-atom cluster, *i.e.*, their binding energy, is further shown in Figure S5 for Co dopants. The binding energy is very strong for Co (> 4 eV). Overall, the DFT calculations suggest that Co dopants show preference to form a three-atom cluster with a central V_S that helps to reduce their oxidation state from +4 as in the perfect MoS_2 lattice. These results are in excellent agreement with the experimental observations, which show a strong preference for forming triangle clusters with a central V_S as the Co concentration increases.

We have further investigated the local magnetic moments due to magnetic interaction within the three-dopant-atom clusters in Co-doped MoS_2. We find that the spins of the three dopant atoms in the cluster are ferromagnetically coupled to each other as shown in the spin-isosurface

plots in Figure S6. Each $3Co_{Mo}+1V_S$ cluster has a magnetic moment of 1 μ_B. We also find that the spin of the neighboring S atoms couples antiferromagnetically to the dopant spins, which suggests an antiferromagnetic superexchange interaction between the dopants and the chalcogens. The delocalized nature of the S 3*p* states, when combined with the antiferromagnetic interaction between the spins of the sulfur atoms and the tri-atom Co clusters, can be expected to result in the effective long-range ferromagnetic coupling between tri-atom clusters that are a few Ångströms apart, especially under an applied magnetic field. Such a superexchange interaction has been theoretically proposed to result in the long-range ferromagnetic coupling between spins of 3*d* transition metals dopants in MoS_2 and other oxides[26, 27].

The tunability of Co concentration in Co-doped MoS_2 monolayers provides an excellent platform to explore the influence of the internal magnetic moments on the valley pseudospin. We studied the valley splitting in Co-doped MoS_2 using polarization-resolved PL in a magnetic field perpendicular to the 2D plane from -7 T to 7 T at a temperature of 4K. Specifically, we only considered the exciton in monolayer MoS_2. The temperature-dependent and laser-power-dependent PL in Co-doped MoS_2 (Figure S7 and FigureS8) confirm that the emission originates from excitons rather than defects[28, 29].

The lattice structure and valley magnetic moments of MoS_2 are shown in Figure S9. **Figures 2**a to **2**c display the normalized PL spectra for the neutral exciton peak in Co-doped MoS_2 with the dopant concentration of 0.8%, at 7 T, 0 T, and −7 T, respectively. At a high field of 7 T (-7 T) (**Figure 2**a and **2**c), the PL spectrum from the +K valley exciton is different to that from the –K valley exciton, indicating valley Zeeman splitting between σ^+ and σ^-. The splitting reaches 3.9 meV at a high field of 7 T (−7 T). In contrast, no splitting is observed at zero field. The zero valley Zeeman splitting at 0 T indicates that time-reversal symmetry is preserved and the

magnetic moments of the Co dopant atoms are randomly oriented. At high magnetic fields, on the other hand, the dopant-atom magnetic moments become ordered, which breaks time invariance and leads to the observed splitting, as shown in **Figure 2**a and **2**c. The normalized PL spectra at different fields from -5T to 5T are presented in Figure S10.

In order to further study the ferromagnetic dopant influence on the valley Zeeman splitting in MoS_2, we also measured the polarized PL under the same conditions in Co-doped MoS_2 monolayers with dopant concentrations of 1.7% and 2.5%. The corresponding results are shown in **Figure 2**d-**2**f and **Figure 2**g-**2**i. It can be clearly seen that the valley Zeeman splitting increases as the dopant concentration increases. The splitting reaches 5.2 meV and 6.15 meV at high magnetic field of 7 T for dopant concentrations of 1.7% and 2.5%, respectively. These results suggest that the Co dopants can effectively tune the valley splitting due to their ferromagnetic coupling to the MoS_2 valley structure. The corresponding valley-exciton Zeeman splitting of MoS_2 with different dopant concentrations as a function of magnetic field from −7 T to 7 T is shown in **Figure 3**a, yielding positive slopes of 0.56 meV/T, 0.71 meV/T and 0.87 meV/T, respectively, for dopant concentrations of 0.8%, 1.7% and 2.5%. More importantly, the Landé g-factors calculated from the valley Zeeman splitting are 9.64, 12.22 and 14.99 for the Co-doped MoS_2 with increasing Co concentration, which are significantly larger than previously reported results in other pristine TMDC monolayers, as shown in supporting information Table S1 [4-9, 15, 30].

In order to obtain a better understanding of the source of the enhanced valley g-factor in the Co-doped MoS_2, we carried out both DFT calculations and a model study. For pristine MoS_2, an applied magnetic field *B* couples to three different magnetic moments: spin, atomic orbital, and valley pseudospin, each of which produces a Zeeman-like splitting in the band energies (**Figure 4**a). Excitations from circularly polarized light conserve spin, whereby the spin-

Zeeman splitting has no net effect on the optical gap. The conduction-band-edge states carry no atomic-orbital angular momentum (m_l = 0), while the valence band edge states do (m_l = 2 at -K and -2 at K), leading to a band shift $|\Delta_a| = 2\mu_B B$. Finally, the valley pseudospin contributes a term given by $\Delta_v = \alpha_c \tau_z \mu_B B$ or $\alpha_v \tau_z \mu_B B$ for the conduction or valence bands[7], where τ_z is the valley pseudospin. The total valley splitting reads

$$\Delta E_0(B) = E_K^0(B) - E_{-K}^0(B) = 2(2 - \Delta\alpha)\mu_B B, \qquad (1)$$

where the index "0" refers to the pristine material without doping. The induced band edge shifts are schematically shown in **Figure 4**a.

For the case of Co doping, atomic-scale STEM analysis has identified both substitutional single dopant and tri-dopant configurations. For the isolated single dopant where a Co atom replaces one Mo atom in the lattice, there are 5 electrons with up spins occupying the 4*d* orbitals of one Mo atom, while 7 electrons on the 3*d* orbitals of a Co atom, leaving 3 up spins occupying m_l = 2, 1, and 0, respectively. Therefore, these substitutional single Co dopants contribute to the localized bonding-reconstruction of the partial states at the valence band edge, but may not lead to an enhancement of the valley splitting as compared to that of pristine MoS_2 (see supporting information Section 2 for a more detailed discussion).

For the tri-dopant case (dominant in our experiment), the three spins are coupled ferromagnetically around a vacancy (Figure S6) so that a local magnetic moment is formed. The carriers' spins have exchange interactions with these local magnetic moments, leading to an internal magnetic field B_{in} under a virtual-crystal approximation[31]. We will show that the presence of the B_{in} explains the giant enhanced valley splitting in our experiment (see supporting information Section 2 for a more detailed discussion). The B_{in}-field interacts not only with the spin degree of freedom, but also with atomic orbital moments and the valley

magnetic moments. In contrast to an applied *B*-field, the B_{in}-field couples to carriers in the conduction and valence bands non-equally so that the B_{in}-field spin-Zeeman splitting has net effect on the optical gap. This non-equal coupling to conduction and valence bands holds for the coupling of the B_{in}-field to the atomic orbital and valley magnetic moments as well. The total valley splitting is included in

$$\Delta E_{\mathrm{inter}} = 2\mu_B\langle S_z\rangle\left\{-x\frac{(N_0\delta)}{\mu_B} + 2x\frac{(N_0\langle J_{AV}\rangle)}{\mu_B} + x\left[-\frac{\alpha_C N_0\langle J_{VC}\rangle}{\mu_B} + \frac{\alpha_V N_0\langle J_{VV}\rangle}{\mu_B}\right]\right\}, \qquad (2)$$

where *x* represents dopant concentration, $\langle S_z\rangle$ indicates the internal magnetic field expressed by an average over local magnetic moments of tri-dopants, $N_0\delta = N_0\beta - N_0\alpha$, $\alpha = \langle \mathrm{KV}|J(\boldsymbol{r})|\mathrm{KV}\rangle$, $\beta = \langle \mathrm{KC}|J(\boldsymbol{r})|\mathrm{KC}\rangle$, $|\mathrm{KV(KC)}\rangle$ indicate the states for the valence (conduction) band in the K valley, and $J(\boldsymbol{r}) = \sum_{\boldsymbol{R}} J(\boldsymbol{r}-\boldsymbol{R})$ describes the s-d exchange interaction between spins and local magnetic moments, $\langle J_{AV}\rangle = \langle KV|J_{AV}|KV\rangle$, $\langle J_{VC}\rangle = \langle KC|J_{VC}|KC\rangle$, $\langle J_{VV}\rangle = \langle KV|J_{VV}|KV\rangle$. Basically, these parameters can be determined by fitting the experimental data in terms of these formulas. To express the physical picture more clearly, we rewrite Eq. (2) as

$$\Delta E_{\mathrm{inter}} = g_{\mathrm{s}}\mu_B B_{\mathrm{in}} + g_a\mu_B B_{\mathrm{in}} + g_{\mathrm{v}}\mu_B B_{\mathrm{in}}, \qquad (3)$$

where $g_{\mathrm{s}}\mu_B B_{\mathrm{in}} = -2x(N_0\delta)\langle S_z\rangle$, $g_a\mu_B B_{\mathrm{in}} = 4x(N_0\langle J_{AV}\rangle)\langle S_z\rangle$, $g_{\mathrm{v}}\mu_B B_{\mathrm{in}} = 2x[-\alpha_C N_0\langle J_{VC}\rangle + \alpha_V N_0\langle J_{VV}\rangle]\langle S_z\rangle$. The band-edge-shifts induced by the B_{in}-field are schematically shown in **Figure 4**(b). For a rough estimation, we assume $N_0\delta = N_0\langle J_{AV}\rangle = N_0\langle J_{VC}\rangle = N_0\langle J_{VV}\rangle$ and the experimental data at 7T, e.g. $x = 0.8\%, k = 0.56\, meV\cdot T^{-1} = 9.675\,\mu_B$; $x = 1.7\%, k = 0.72\, meV\cdot T^{-1} = 12.440\,\mu_B$; $x = 2.5\%, k = 0.87\, meV\cdot T^{-1} = 15.031\,\mu_B$, and arrive at $N_0\delta \approx -0.5$ eV, which is comparable to those found in dilute magnetic semiconductors[32].

In summary, we have successfully synthesized MoS_2 monolayers doped with magnetic Co atoms via CVD method. Atomic-scale electron microscopy studies confirm that the Co atoms substitute the Mo sites within the lattice, where isolated single dopants and tri-dopant clusters

with a central sulfur vacancy are formed, as confirmed by DFT calculations. We find that an internal magnetic field B_{in} is formed by the tri-dopants, which couples to the spin, atomic orbital, and valley magnetic moment of carriers from conduction and valence bands. The coupling of spin with the B_{in} field is distinct to that for an external magnetic field B. The B_{in}-field affects the PL shift, while the external B-field does not. The internal magnetic field results in a giant enhancement of the valley splitting, stemming from the inherent overlap of carrier and impurity wave functions. Our results demonstrate a possible way to tune the valley pseudospin in TMDCs by magnetic atom doping. The large valley Zeeman splitting makes Co-doped MoS_2 a promising candidate for magneto-optical and spintronic device applications.

Experimental Section

Synthesis of MoS_2 and Co-doped MoS_2: Pure MoS_2 and doped MoS_2 were synthesized by CVD method using MoO_3 and sulfur (Sigma) as the reaction sources. $CoCl_2$ was used as the dopant source. The pure MoS_2 and doped-MoS_2 were synthesized in quartz tubes (1-inch diameter) under temperature ranging from 700 to 750 ^oC. The setup for the growth is shown in Figure S1. Specifically, for the pure MoS_2, Ar flow of 80 sccm was used as the carrier gas and a silicon boat contained 10 mg MoO_3 was put in the center of the tube. The SiO_2/Si substrate is placed on the boat with the surface downside. Another silicon boat containing 0.5 g S powder was located on the upstream. The temperature ramped up to 750 ^oC in 15 min, and was kept at the reaction temperature for about 5 min to 10 min. Then the furnace was cooled down to room temperature gradually. For the Co-doped MoS_2, the boat containing mixed powder of $CoCl_2$ and MoO_3 (mole ratio of 1: 99, 2: 98, 3: 97 and 6 for Co-doped MoS_2) was put in the center of the tube. The reaction condition was similar to the synthesis of pure MoS_2, except that it used mixed Ar/H_2 with a flow of 80/5 sccm as the carrier gas.

Raman and Photoluminescence (PL) Characterization: Room temperature Raman and PL measurements with an excitation laser of 532 nm were performed using a WITEC alpha 300R Confocal Raman system. Before Raman characterization, the system was calibrated with the Raman peak of Si at 520 cm^{-1}. The laser powers are less than 1mW to avoid overheating of the samples.

PL measurements at 4K: We used a homemade fiber-based confocal microscope for polarization-resolved PL spectroscopy. The wavelength of the excitation is 532 nm. The excitation power is ~270 μW within a spot of ~1 μm in diameter. Polarizers and quarter wave plates are installed to generate and detect circular polarization. The PL emission is collected into a spectrometer (Andor Shamrock 500i) with a CCD camera via a multi-mode fiber for spectroscopy recording. The sample is placed in a magneto-cryostat in a Faraday geometry and cooled down to 4 K. The magnetic field up to 7 T is perpendicular to the sample plane. Note that all the spectra for all magnetic fields have been fitted using Gaussian functions. The peak positions from the Gaussian fitting were used to calculate the valley splitting, and the errors were taken as the error bars in Figure 3a.

STEM Characterization: The TEM samples were prepared with a poly (methyl methacrylate) (PMMA) assisted method. A layer of PMMA of about 1 μm thick was spin-coated on the wafer with doped MoS_2 samples deposited and then baked at 180 °C for 3min. Afterward, the wafer was immersed in NaOH solution (1M) to etch the SiO_2 layer overnight. After lift-off, the doped MoS_2 sample was transferred into DI water for several cycles to wash away the residual contaminants, and then it was fished by a TEM grid (Quantifoil Mo grid). The as-transferred specimen was dried naturally in the ambient environment, and then dropped into acetone overnight to wash away the PMMA coating layers. The STEM analysis was performed on an aberration-corrected JEOL 2100F with a cold field-emission gun and an aberration corrector

(the DELTA-corrector), operating at 60 kV. All STEM experiments were performed at room temperature.

Density Functional Theory (DFT) Calculations: DFT calculations were performed using a plane-wave basis set with cut-off energy of 450 eV and the projector-augmented-wave (PAW)[33] method as implemented within the Vienna *Ab initio* Simulation Package (VASP)[34, 35]. Exchange and correlation effects were described within the Generalized Gradient Approximation (GGA) in the Perdew–Burke–Ernzerhof (PBE) parameterization[36]. We used a 5 × 5 × 1 supercell of the MoS_2 primitive cell with ~20 Å vacuum to simulate monolayer MoS_2. To check the convergence of the results with respect to supercell size, some calculations were repeated using a larger 7 × 7 × 1 supercells. We used a 3 × 3 × 1 Γ-centered Monkhorst-Pack (MP) grid[37] for structural relaxations where only the atomic positions were optimized, and (5 × 5 × 1) *k*-points mesh was used for the electronic calculation. The formation energy (E_f) of the dopant structure in a 25 formula unit MoS_2 supercell, for instance, a transition metal-substituted MoS_2 without or with a sulfur vacancy: $TM_xMo_{25-x}S_{50-y}$, is described as[38]:

$$E_f = \frac{E(\mathrm{TM_xMo_{25\text{-}x}S_{50\text{-}y}}) + x(\mu_{\mathrm{Mo}} - \mu_{\mathrm{MT}}) + y\mu_s - 25E(\mathrm{MoS_2})}{x} \quad (4)$$

where, $E\left(\mathrm{TM}_x\mathrm{Mo}_{25-x}\mathrm{S}_{50-y}\right)$ is the DFT total energy of the dopant structure, $E\left(\mathrm{MoS_2}\right)$ is the total energy of one formula unit of MoS_2 and μ_i is the chemical potential of element *i*. The formation energy as defined in Eq. 3 is expressed per TM dopant atom. Experimentally, as the transition metals substitute Mo atoms, we consider the growth conditions to be Mo-poor or S-rich. Hence, we define μ_S as half the energy of a S_2 molecule as obtained by DFT and $\mu_{Mo} = E(MoS_2) - 2\mu_S$. μ_{TM} is further defined as the difference in energy between the most stable form of the transition metal sulfide (TM_xS_y) as obtained from the Materials Project Database[39] and

μ_S. The most stable sulfides for V, Cr, Mn, Fe, Co, and Ni are V_3S_4, Cr_2S_3, MnS_2 (hexagonal form), FeS_2, Co_3S_4, and Ni_3S_4, respectively.

To investigate the tendency of a transition metal dopant to form a tri-atom cluster, we used the binding energy E_b, which is defined as:

$$E_b = 3E(\mathrm{TM_1Mo_{24}S_{50}}) - E(\mathrm{TM_3Mo_{22}S_{50}}) - 50E(\mathrm{MoS_2}) \quad (5)$$

In Eq. 4, a positive binding energy suggests a tendency to form a tri-atom cluster.

Supporting Information
Supporting Information is available from the Wiley Online Library or from the author.

Acknowledgements

This work is supported by the Singapore National Research Foundation under NRF RF Award No. NRF-RF2013-08, AcRF Tier 1 RG4/17 and RG7/18, AcRF Tier 3 2018-T3-1-002, The National Research Foundation (NRF) Competitive Research Programme (CRP) Funding NRF-CRP21-2018-0007, and the A*Star QTE programme. National Key R&D Program of China (2018YFA0305800), the Natural Science Foundation of China (51622211, 11674317), and the Key Research Program of Frontier Sciences of Chinese Academy of Sciences. J.L. and K.S. acknowledge JST-ACCEL and JSPS KAKENHI (JP16H06333 and P16823) for financial support. This research was also supported in part by U.S. DOE grant DE-FG02-09ER46554 (HS, JAB, STP). Work at Washington University (RM) was supported by National Science Foundation grant number CBET-**1729787**. This work used computational resources of the Extreme Science and Engineering Discovery Environment (XSEDE), which is supported by National Science Foundation grant number ACI-1053575, and of the National Energy Research Scientific Computing Center, a DOE Office of Science User Facility supported by the Office of Science of the U.S. Department of Energy under Contract No. DE-AC02-05CH11231.

Received: ((will be filled in by the editorial staff))
Revised: ((will be filled in by the editorial staff))
Published online: ((will be filled in by the editorial staff))

Reference

[1] J. Lee, K. F. Mak, J. Shan, *Nat Nanotechnol* **2016**, 11, 421.
[2] H. T. Yuan, M. S. Bahramy, K. Morimoto, S. F. Wu, K. Nomura, B. J. Yang, H. Shimotani, R. Suzuki, M. Toh, C. Kloc, X. D. Xu, R. Arita, N. Nagaosa, Y. Iwasa, *Nat Phys* **2013**, 9, 563.
[3] Y. Ye, J. Xiao, H. L. Wang, Z. L. Ye, H. Y. Zhu, M. Zhao, Y. Wang, J. H. Zhao, X. B. Yin, X. Zhang, *Nat Nanotechnol* **2016**, 11, 597.
[4] A. Arora, R. Schmidt, R. Schneider, M. R. Molas, I. Breslavetz, M. Potemski, R. Bratschitsch, *Nano Lett* **2016**, 16, 3624.
[5] A. Srivastava, M. Sidler, A. V. Allain, D. S. Lembke, A. Kis, A. Imamoglu, *Nat Phys* **2015**, 11, 141.

[6] G. Wang, L. Bouet, M. M. Glazov, T. Amand, E. L. Ivchenko, E. Palleau, X. Marie, B. Urbaszek, *2D Mater* **2015**, 2, 034002.
[7] G. Aivazian, Z. R. Gong, A. M. Jones, R. L. Chu, J. Yan, D. G. Mandrus, C. W. Zhang, D. Cobden, W. Yao, X. Xu, *Nat Phys* **2015**, 11, 148.
[8] Y. L. Li, J. Ludwig, T. Low, A. Chernikov, X. Cui, G. Arefe, Y. D. Kim, A. M. van der Zande, A. Rigosi, H. M. Hill, S. H. Kim, J. Hone, Z. Q. Li, D. Smirnov, T. F. Heinz, *Phys Rev Lett* **2014**, 113, 148.
[9] A. V. Stier, K. M. McCreary, B. T. Jonker, J. Kono, S. A. Crooker, *Nat Commun* **2016**, 7, 10643.
[10] F. Cadiz, E. Courtade, C. Robert, G. Wang, Y. Shen, H. Cai, T. Taniguchi, K. Watanabe, H. Carrere, D. Lagarde, M. Manca, T. Amand, P. Renucci, S. Tongay, X. Marie, B. Urbaszek, *Phys Rev X* **2017**, 7, 021026.
[11] A. A. Mitioglu, P. Plochooka, A. G. del Aguila, P. C. M. Christianen, G. Deligeorgis, S. Anghel, L. Kulyuk, D. K. Maude, *Nano Lett* **2015**, 15, 4387.
[12] A. A. Mitioglu, K. Galkowski, A. Surrente, L. Klopotowski, D. Dumcenco, A. Kis, D. K. Maude, P. Plochocka, *Phys Rev B* **2016**, 93, 165412.
[13] A. V. Stier, N. P. Wilson, G. Clark, X. D. Xu, S. A. Crooker, *Nano Lett* **2016**, 16, 7054.
[14] Q. Y. Zhang, S. Y. A. Yang, W. B. Mi, Y. C. Cheng, U. Schwingenschlogl, *Adv Mater* **2016**, 28, 959.
[15] T. N. Chuan Zhao, Puqin Zhao, Yingchun Cheng, Peiyao Zhang, Fan Sun, Payam Taheri, Jieqiong Wang, Yihang Yang, Thomas Scrace, Kaifei Kang, Sen Yang, Guo-xing Miao, Renat Sabirianov, George Kioseoglou, Athos Petrou, Hao Zeng, *Nat Nanotechnol* **2017**, 757.
[16] D. Zhong, K. L. Seyler, X. Y. Linpeng, R. Cheng, N. Sivadas, B. Huang, E. Schmidgall, T. Taniguchi, K. Watanabe, M. A. McGuire, W. Yao, D. Xiao, K. M. C. Fu, X. D. Xu, *Sci Adv* **2017**, 3, e1603113.
[17] W. B. Xu, P. Li, S. S. Li, B. J. Huang, C. W. Zhang, P. J. Wang, *Physica E* **2015**, 73, 83.
[18] J. S. Qi, X. Li, X. F. Chen, K. G. Hu, *J Phys-Condens Mat* **2014**, 26, 256003.
[19] X. L. Fan, Y. R. An, W. J. Guo, *Nanoscale Res Lett* **2016**, 11, 154.
[20] R. Mishra, W. Zhou, S. J. Pennycook, S. T. Pantelides, J. C. Idrobo, *Phys Rev B* **2013**, 88, 144409.
[21] K. H. Zhang, S. M. Feng, J. J. Wang, A. Azcatl, N. Lu, R. Addou, N. Wang, C. J. Zhou, J. Lerach, V. Bojan, M. J. Kim, L. Q. Chen, R. M. Wallace, M. Terrones, J. Zhu, J. A. Robinson, *Nano Lett* **2015**, 15, 6586.
[22] B. Li, L. Huang, M. Z. Zhong, N. J. Huo, Y. T. Li, S. X. Yang, C. Fan, J. H. Yang, W. P. Hu, Z. M. Wei, J. B. Li, *Acs Nano* **2015**, 9, 1257.
[23] A. W. Robertson, Y. C. Lin, S. S. Wang, H. Sawada, C. S. Allen, Q. Chen, S. Lee, G. D. Lee, J. Lee, S. Han, E. Yoon, A. I. Kirkland, H. Kim, K. Suenaga, J. H. Warner, *ACS Nano* **2016**, 10, 10227.
[24] A. Ramasubramaniam, D. Naveh, *Phys Rev B* **2013**, 87, 195201.
[25] W. Zhou, X. L. Zou, S. Najmaei, Z. Liu, Y. M. Shi, J. Kong, J. Lou, P. M. Ajayan, B. I. Yakobson, J. C. Idrobo, *Nano Lett* **2013**, 13, 2615.
[26] A. N. Andriotis, M. Menon, *Phys Rev B* **2013**, 87, 155309.
[27] A. N. Andriotis, M. Menon, *Phys Rev B* **2014**, 90, 125304.
[28] Y. M. He, G. Clark, J. R. Schaibley, Y. He, M. C. Chen, Y. J. Wei, X. Ding, Q. Zhang, W. Yao, X. D. Xu, C. Y. Lu, J. W. Pan, *Nat Nanotechnol* **2015**, 10, 497.
[29] A. Srivastava, M. Sidler, A. V. Allain, D. S. Lembke, A. Kis, A. Imamoglu, *Nat Nanotechnol* **2015**, 10, 491.
[30] D. MacNeill, C. Heikes, K. F. Mak, Z. Anderson, A. Kormanyos, V. Zolyomi, J. Park, D. C. Ralph, *Phys Rev Lett* **2015**, 114, 037401.
[31] J. SINOVA, *Int J Mod Phys B* **2004**, 18, 1083.

[32] J. K. Furdyna, *J Appl Phys* **1988**, 64, R29.
[33] P. E. Blochl, *Phys Rev B* **1994**, 50, 17953.
[34] G. Kresse, J. Hafner, *Phys Rev B* **1993**, 47, 558.
[35] G. Kresse, J. Furthmuller, *Phys Rev B* **1996**, 54, 11169.
[36] J. P. Perdew, K. Burke, M. Ernzerhof, *Phys Rev Lett* **1996**, 77, 3865.
[37] H. J. Monkhorst, J. D. Pack, *Phys Rev B* **1976**, 13, 5188.
[38] S. B. Zhang, J. E. Northrup, *Phys Rev Lett* **1991**, 67, 2339.
[39] A. Jain, S. P. Ong, G. Hautier, W. Chen, W. D. Richards, S. Dacek, S. Cholia, D. Gunter, D. Skinner, G. Ceder, K. A. Persson, *Apl Mater* **2013**, 1, 011002.

Figure and Figure Caption

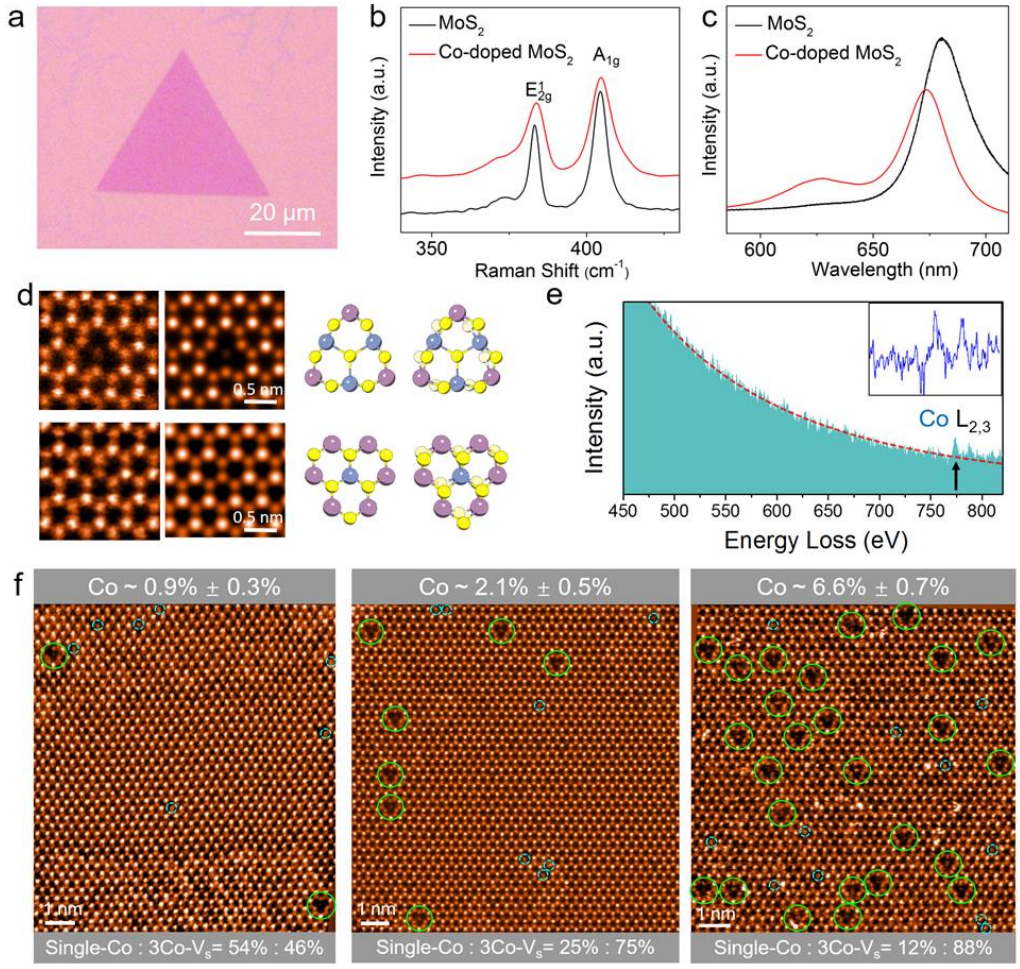

Figure 1 Structural characterizations of Co-doped MoS_2. a, Optical image of Co-doped MoS_2, with a doping concentration of ~1%. b and c, Raman and PL spectra of the corresponding Co-doped MoS_2. The spectra of pristine MoS_2 monolayer are provided for comparison. The presence of the A_g mode around ~ 401 cm^{-1} and the E_g mode around ~ 381 cm^{-1} indicate that

the MoS_2 structure preserves despite the small dopant concentration. It can be clearly seen that two PL peaks of Co-doped MoS_2 at 625 nm and 675 nm are observed. The PL peak locating 625 nm at room temperature originates from the B exciton. d, Experimental atom-resolved ADF-STEM and simulated STEM images along with the corresponding structural models of the two types of dopant configurations found in Co-doped MoS_2. The images reveal the presence of isolated single dopants and tri-dopant clusters substituted in the Mo sites in Co-doped MoS_2. The slightly tilted atomic models on the right are shown for direct visualization of the di-sulphur columns. e, The corresponding single-atom EELS analysis of the dopants shown in (d). The red dashed lines indicate the background signal. The insets are the enlarged background subtracted EELS of Co $L_{2,3}$ edges. f, Typical ADF-STEM images of Co-doped MoS_2 monolayers with different dopant concentrations. The single isolated Co dopant and tri-dopant are highlighted by light blue and green circles, respectively. The Co concentration is estimated by statistical analysis of random regions sampled across the same flake where the presented ADF-STEM images were taken. The relative population ratio of the two dopant configurations is listed below the corresponding images. The appearance of the tri-dopant cluster becomes dominant as the dopant concentration increases.

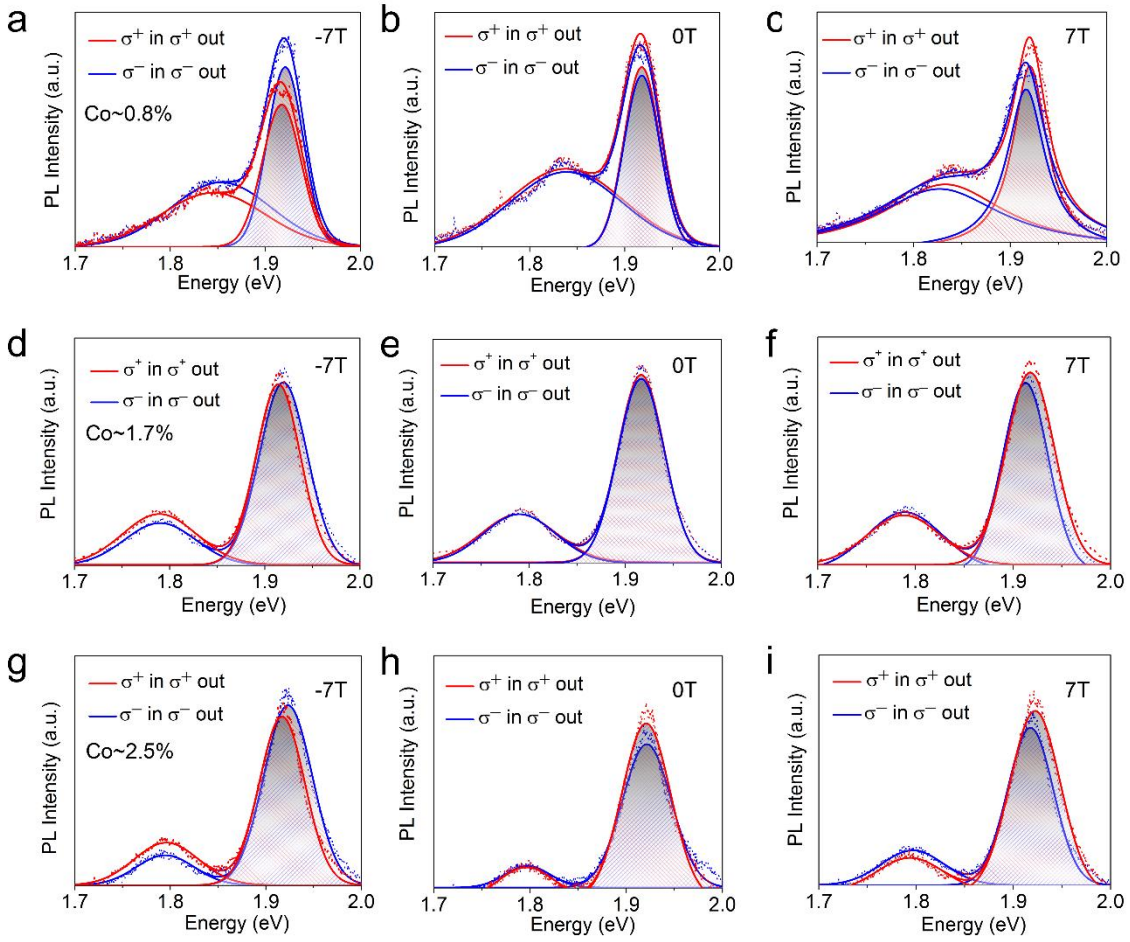

Figure 2 Valley Zeeman splitting in Co-doped MoS_2 with different dopant concentration. a-i, Polarization-resolved valley-exciton PL of Co-doped MoS_2 at -7T, 0T and 7T, respectively, with Co concentrations of 0.8% (a-c), 1.7% (d-f) and 2.5% (g-i). Red and blue curves represent PL spectra when excited and detected with a single helicity, corresponding to the K and -K valleys, respectively. Dots: raw data; curves: Gaussian fitted results.

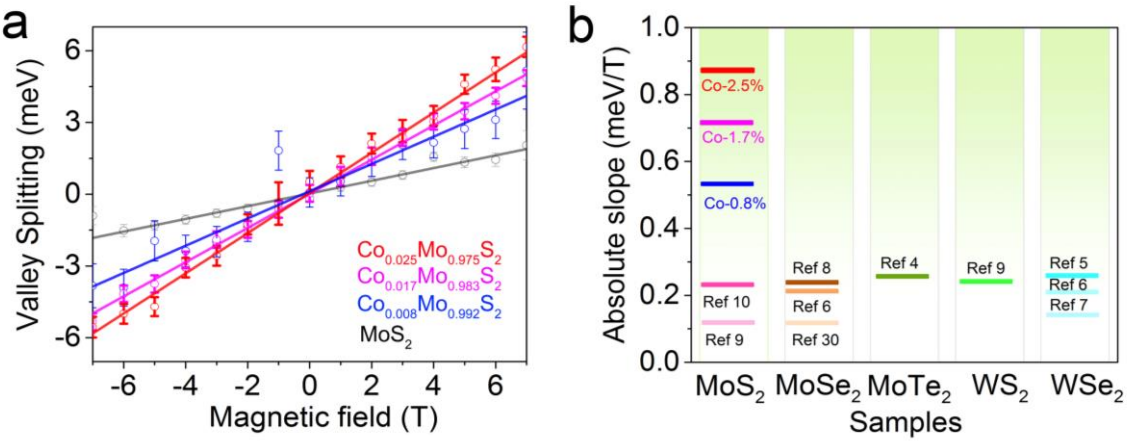

Figure 3 Comparison of the magnitude of valley splitting in Co-doped MoS_2 with different dopant concentrations. a, Zeeman valley splitting as a function of the magnetic field in Co-doped MoS_2 with different dopant concentrations from -7T to 7T. The pristine MoS_2, Co concentrations of 0.8% (blue), 1.7% (magenta), and 2.5% (red) correspond to a slope of 0.26 $meVT^{-1}$, 0.56 $meVT^{-1}$, 0.72 $meVT^{-1}$, and 0.87 $meVT^{-1}$, respectively. b, Comparisons of the Zeeman valley splitting slops in different samples in current literature. The Zeeman valley splitting in Co-doped MoS_2 is larger than reported values in pristine MoS_2[9, 10], $MoSe_2$[6, 8, 30], WS_2[9], pristine WSe_2[5-7] and pristine $MoTe_2$[4]. It can be clearly seen that the Zeeman valley splitting increases as the dopant concentration increases in Co-doped MoS_2, indicating that the Co doping can effectively tune the Zeeman valley in MoS_2.

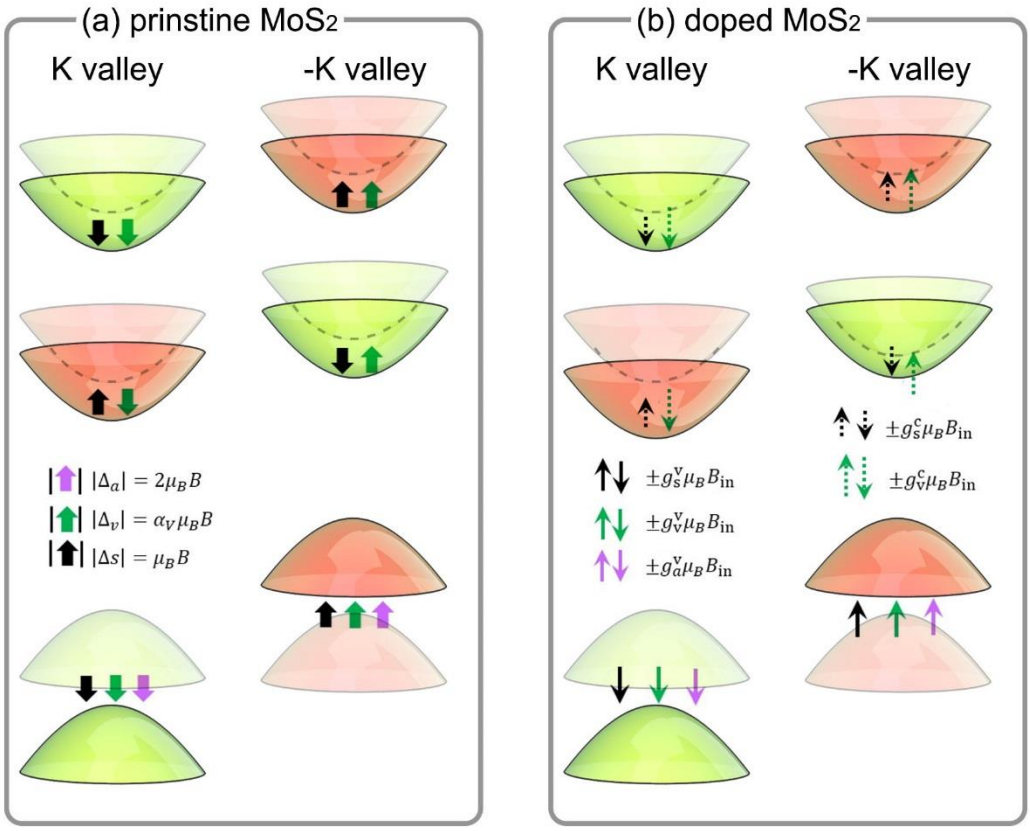

Figure 4 Schematic illustration of the Zeeman-like splitting induced by the internal magnetic field for doped MoS_2. A comparison is shown for pristine MoS_2 in (a). In principle, the internal magnetic field in doped MoS_2 couples to the conduction band and valence band

non-equally, which is distinct to the external magnetic field. Therefore, the shifts of the optical gap are related to the relative difference of the effects on the conduction and valence bands. The superscripts of "c" and "v" in the g-factors represent the conduction and valence bands, respectively. The subscripts of "s", "a" and "v" in the g-factors refer to spin, atomic orbital moment, and valley magnetic moment, respectively.

Co-doped MoS_2 monolayer, showing enhanced valley splitting, was synthesized by CVD method. We show that internal magnetic moments induced by magnetic dopants in MoS_2 monolayers serves as a new means to engineer the valley Zeeman splitting (VZS). Specifically, we report the successful synthesis of monolayer MoS_2 doped with magnetic element Co, and engineer the magnitude of valley splitting by manipulating the dopant concentration. Valley splittings of 3.9 meV, 5.2 meV and 6.15 meV at 7 T in Co-doped MoS_2 with Co concentrations of 0.8%, 1.7% and 2.5%, respectively, are achieved as revealed by polarization-resolved photoluminescence (PL) spectroscopy. Atomic-resolution electron microscopy studies clearly identify the magnetic sites of Co substitution in the MoS_2 lattice, forming two distinct types of configurations, namely isolated single dopants and tri-dopant clusters. Density-functional-theory and model calculations reveal that the observed enhanced VZS arises from an internal magnetic field induced by the tri-dopant clusters, which couples to the spin, atomic orbital, and valley magnetic moment of carriers from the conduction and valence bands. The present study demonstrates a new method to control the valley pseudospin via magnetic dopants in layered semiconducting materials, paving the way towards magneto-optical and spintronic devices.

Keywords: MoS_2, chemical vapor deposition, Co-doped, valley splitting, two-dimensional materials

Jiadong Zhou, Junhao Lin, Hunter Sims, Chongyun Jiang, Chunxiao Cong, John A. Brehm, Zhaowei Zhang, Lin Niu, Yu Chen, Yao Zhou, Yanlong Wang, Fucai Liu, Chao Zhu, Ting Yu, Kazu Suenaga, Rohan Mishra, Sokrates T. Pantelides, Zhen-Gang Zhu, Weibo Gao, Zheng Liu, and Wu Zhou

Synthesis of Co-doped MoS_2 monolayer with enhanced valley splitting

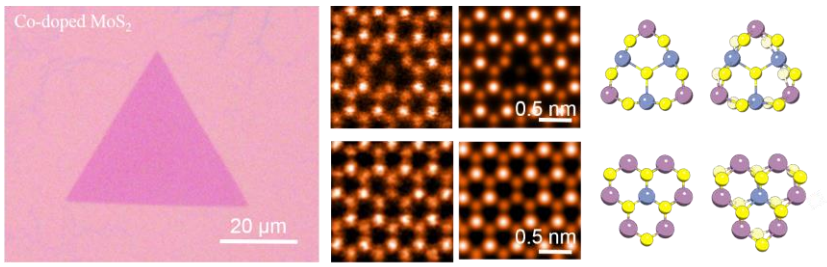

Supporting Information

Synthesis of Co-doped MoS_2 monolayer with enhanced valley splitting

Jiadong Zhou, Junhao Lin, Hunter Sims, Chongyun Jiang, Chunxiao Cong, John A. Brehm, Zhaowei Zhang, Lin Niu, Yu Chen, Yao Zhou, Yanlong Wang, Fucai Liu, Chao Zhu, Ting Yu, Kazu Suenaga, Rohan Mishra, Sokrates T. Pantelides, Zhen-Gang Zhu, Weibo Gao, Zheng Liu, and Wu Zhou

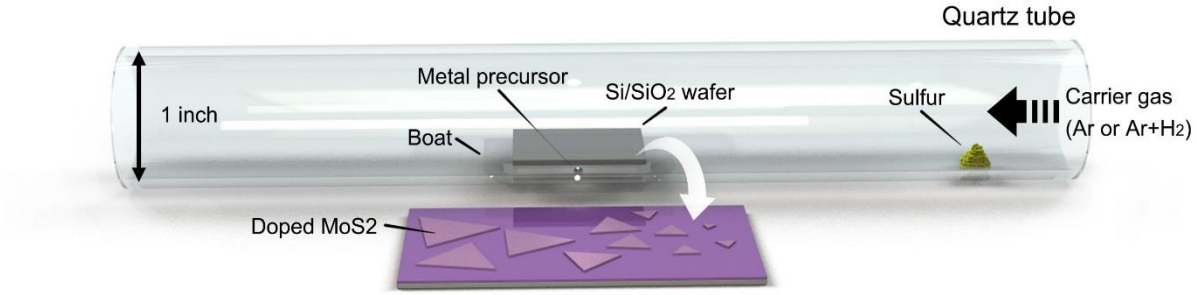

Figure S1 The growth setup used for the synthesis of pure MoS_2 and doped MoS_2. $CoCl_2$ was used as the dopant source for Co-doped MoS_2. The sulfur powder and MoO_3 were used as the S and Mo sources. The synthesis was conducted in a quartz tube (1-inch diameter) with the growing temperature from 700 to 800 ^oC.

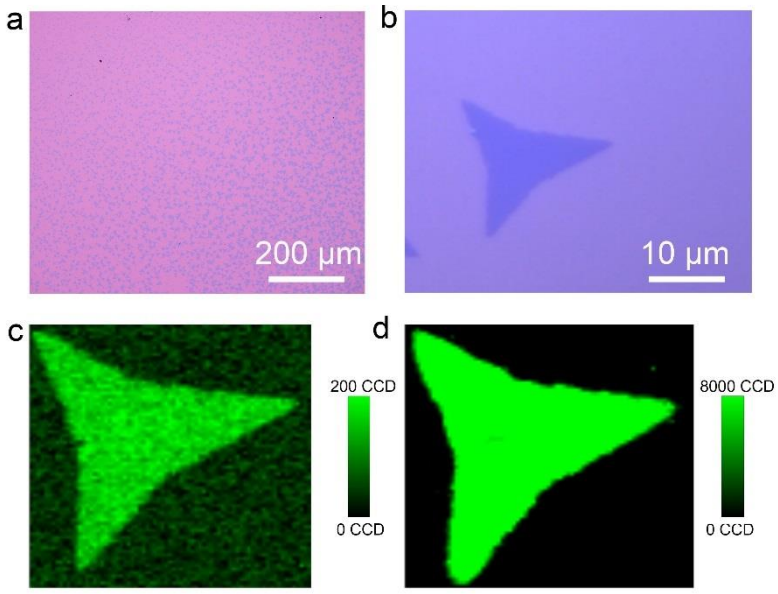

Figure S2 Optical image and Raman/PL mapping of Co-doped MoS_2. a, Optical image of Co-doped MoS_2 on a large scale wafer. b, Optical image of Co-doped MoS_2 used for Raman and PL measurement. c and d, Raman mapping (A_{1g} mode) and PL mapping of Co-doped MoS_2.

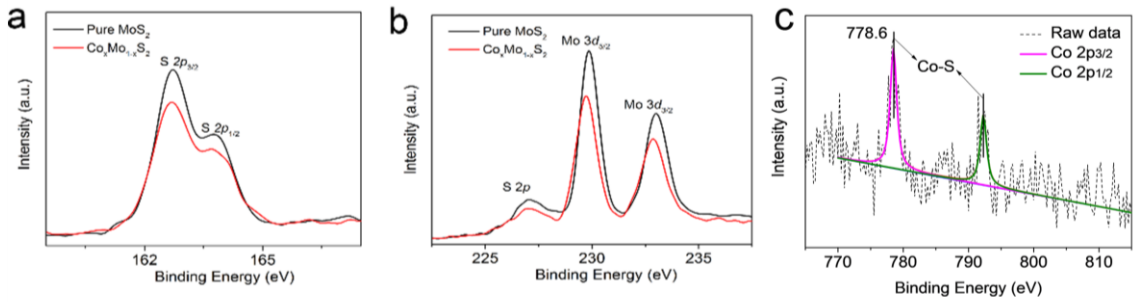

Figure S3 XPS spectra of Co-doped MoS_2. XPS spectra of S ($2p_{3/2}$, $2p_{1/2}$) (a), Mo ($3d_{5/2}$, $3d_{5/2}$) (b), and Co ($2p_{3/2}$, $2p_{1/2}$) (c) edges in Co-doped MoS_2. The Mo edges in the Co-doped sample show a slight shift from that in pristine MoS_2. The XPS results of the high-resolution Co 2p spectrum shows that the peak of Co $2p_{3/2}$ at 778.6 eV corresponding to the Co-S bonding, no peak assigned to the CoMoS phase (Co $2p_{3/2}$ at 779.2 eV) being found in the Co-doped MoS_2 [1-3]. From XPS data, the atomic ratio of Co 3*d*: Mo 3*d*: S 3*d* is 0.6: 34.3: 65.1, thus the atomic ratio of S to Co/Mo can be estimated to be 65.1 / (0.6 + 34.3) ~ 1.87, which is a slightly lower than the ideal stoichiometric value of 2. This is attributed to the S vacancy in Co-doped MoS_2 samples. The Co concentration and S vacancy have been further confirmed by the STEM.

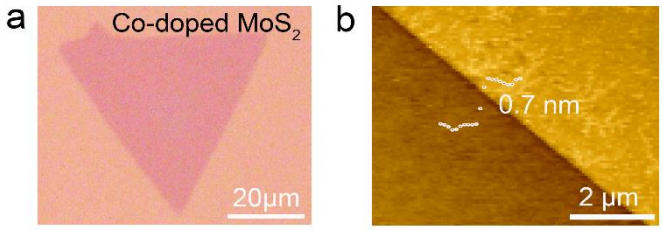

Figure S4 Optical image and AFM image of Co-doped MoS_2. a, Optical image of Co-doped MoS_2. b, AFM image of Co-doped MoS_2. The thickness of 0.7 nm confirms the monolayer nature of the as-synthesized Co-doped MoS_2.

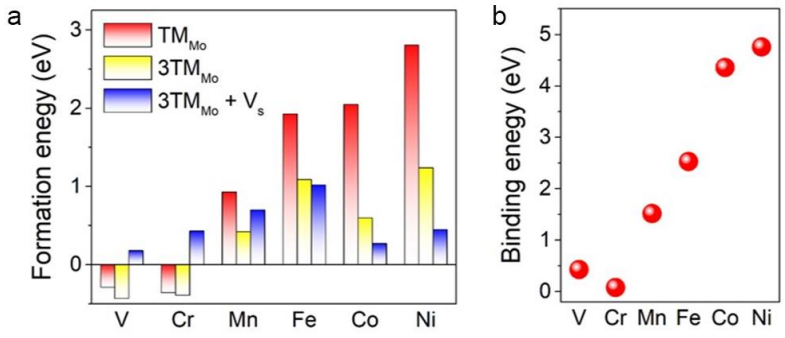

Figure S5 Formation energy and binding energy of different transition metals in MoS_2. a, Formation energy of single dopants and tri-dopant clusters with and without central sulfur vacancies in MoS_2 doped with different magnetic elements. b, Binding energy of different elements in the tri-dopant cluster configuration.

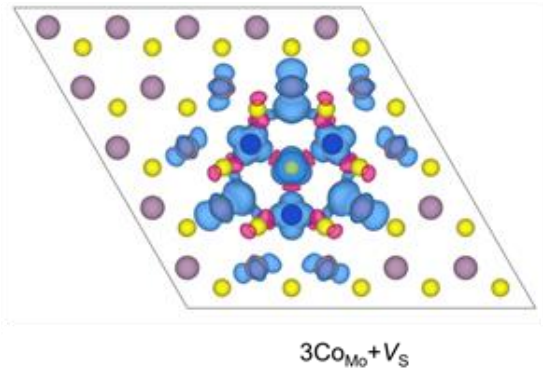

Figure S6 Local magnetism in Co-doped MoS_2 monolayer. Isosurface plots showing the spin density around $3Co_{Mo}+1V_S$, with blue representing majority spin and magenta minority spin. Neighboring Mo and S sites also exhibit some magnetization, giving a total moment of 1 μ_B per triangle for Co. The sulfur spins are predominantly aligned antiparallel to the spins on the transition metal clusters. The isosurface value was taken at 0.001 *e*/Å[3].

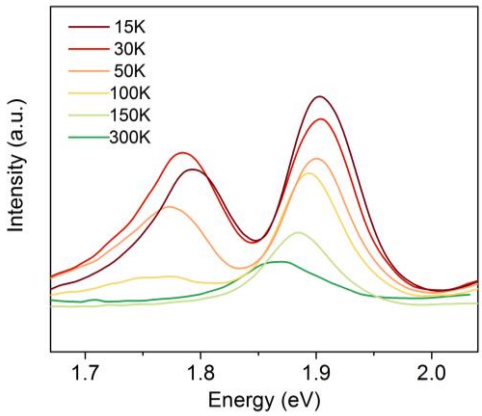

Figure S7 Temperature-dependent PL in Co-doped MoS_2. PL spectra of Co-doped MoS_2 monolayer (Co ~ 2.5%) taken at temperatures from 300 K to 15 K. The PL peak position blue-shifts as the temperature decreases. With the temperature decreasing, the PL (1.77 eV) originating from local defect appears. This is similar to the reported results[4].

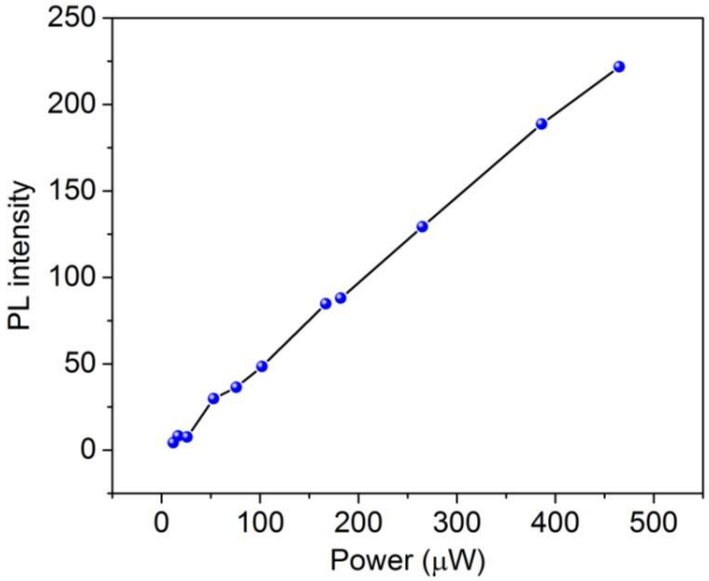

Figure S8 Laser power-dependent PL in Co-doped MoS_2. PL spectra of Co-doped MoS_2 (Co ~ 2.5%) taken under different laser power. The linear relationship between the laser power and PL intensity indicates that the PL originates from the exciton instead of defects[5,6].

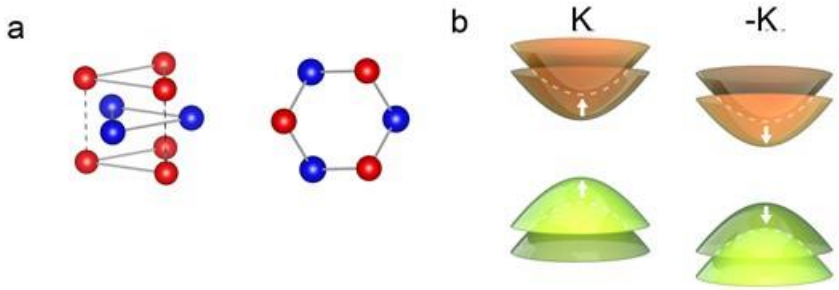

Figure S9 The lattice structure and valley magnetic moments of MoS_2 monolayer. a, Schematic of the lattice structure of monolayer MoS_2 and the broken inversion symmetry. b, Schematic valley structure of MoS_2 near the K and −K points in the absence of a magnetic field, showing the optical selection rules for the A exciton transition studied in this experiment.

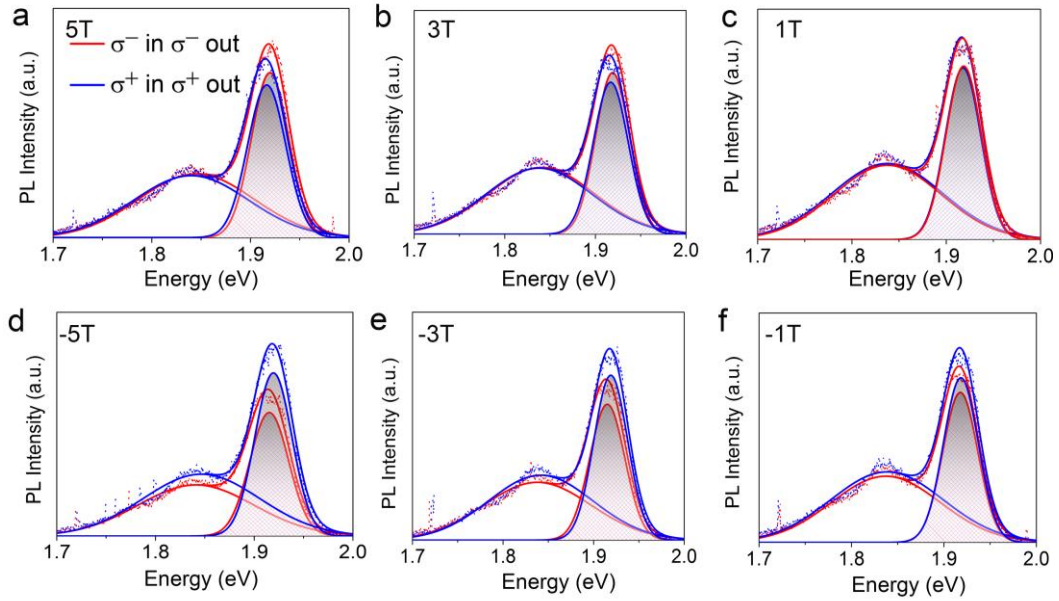

Figure S10 Polarization-resolved valley-exciton PL in Co-doped MoS_2 with a Co concentration of 0.8%. (a-c) Polarization-resolved PL spectra in Co-doped MoS_2 at 5T (a), 3T (b), 1T (c), -5T (d), -3T (e), and -1 T (f), respectively.

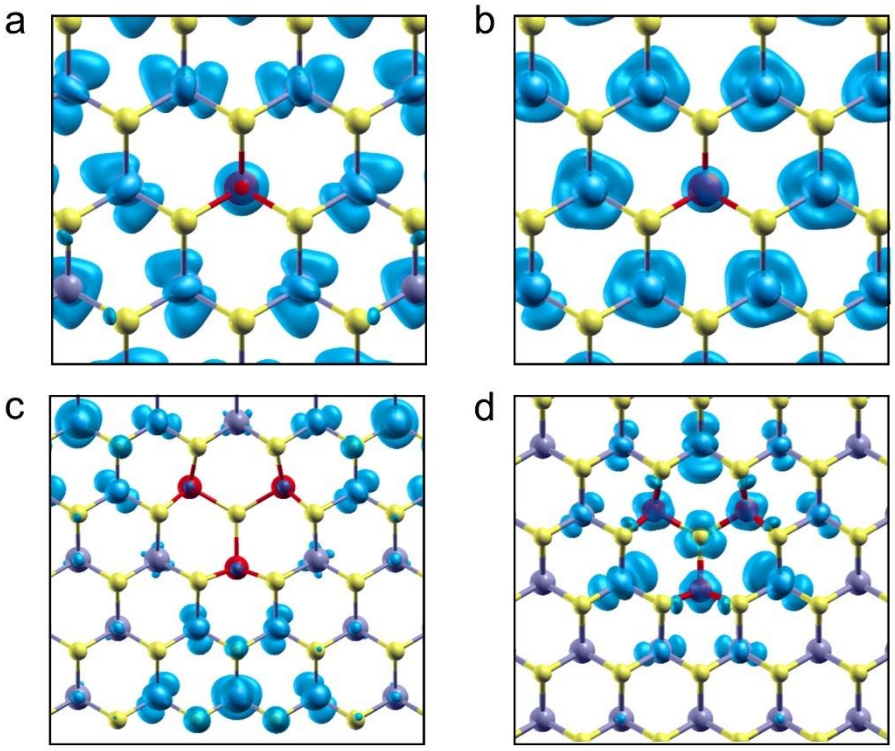

Figure S11 Charge density of MoS_2 with an isolated Co dopant and a tri-dopant cluster. a-b, Excitations in MoS_2 with an isolated Co dopant. The charge density of the (a) valence and (b) conduction bands shows a transition from a state containing $m = \pm 2$ contributions (containing *xy* lobes) to one containing a large $m = 0$ character (resembling $3z^2$-r^2 atomic orbitals). c-d, Excitations in MoS_2 with $3Co_{Mo}$+V_S clusters. Here, (c) and (d) show the real-space location of the valence and conduction band edges, respectively. The situation is now reversed, with the valence band containing more $m = 0$ character and arises from states away from the dopant cluster, while the conduction band exhibits large lobes directed along the *xy* direction (containing non-zero orbital momentum).

Table S1 Summary of effective *g*-factors in monolayer TMDs[7-12].

Material	A exciton *g*-factor
Monolayer MoS_2	-3.94/-1.7/-4
Monolayer WS_2	-4.0
Monolayer $MoSe_2$	-3.8 / -4.1
Monolayer WSe_2	-3.7/-4.37/-1.7/-4
Monolayer $MoTe_2$	4.2
$Mo_{0.992}Co_{0.008}S_2$	9.64
$Mo_{0.983}Co_{0.017}S_2$	12.22
$Mo_{0.975}Co_{0.025}S_2$	14.99

Section 2. Theory for the enhanced valley splitting due to the magnetic dopants

2.1. Valley splitting for pristine MoS_2

Summarizing the explanation appearing in Ref. 6 for pristine MoS_2, an applied magnetic field *B* couples to three different magnetic moments: spin, atomic orbital, and valley pseudospin, each of which produces a Zeeman-like splitting in the band energies. Excitations from circularly polarized light conserve spin, whereby the spin-Zeeman splitting has no net effect on the optical gap. In pristine MoS_2, the conduction-band-edge states carry no atomic-orbital angular momentum (m_l = 0), while the valence band edge states do (m_l = 2 at -K and -2 at K). This causes the band with non-zero m_l to move with respect to the other edge, giving the optical gap a field dependence of $\pm 2\mu_B B$, where the sign depends on whether the orbital moment lies in the K (+) or -K (-) valley. Finally, the valley pseudospin contributes a term given by $\Delta_v = \alpha\tau_z\mu_B B$, where τ_z is the valley pseudospin, and **k**·**p** theory shows that the effective g-factor α depends on the effective masses of the band edge and neighboring bands. If the g-factors for the valence and conduction bands differ (and differ between valleys), additional splitting is generated. For pristine MoS_2, the optical gap for K valley is given by

$$E_K^0(B) = E_{g,b} - E_{bind,ex} - m\mu_B B + \Delta\alpha\tau_z\mu_B B = \Delta^0 + (2 - \Delta\alpha)\mu_B B, \qquad (1)$$

$$E_{-K}^{0}(B) = \Delta^{0} - (2 - \Delta\alpha)\mu_B B, \quad (2)$$

where $E_{g,b}$ is the band gap, $E_{bind,ex}$ is the binding energy of the X^0 exciton, and $\Delta\alpha = \alpha_c - \alpha_v$ is the difference of the g-factor between the conduction and valence band. The total shift in the PL peaks (the difference between the peak shifts in the K and -K valley) reads

$$\Delta E_0(B) = E_K^0(B) - E_{-K}^0(B) = 2(2 - \Delta\alpha)\mu_B B, \quad (3)$$

where the index "0" means the situation without doping.

2.2. Valley splitting stemming from the band modifications due to the dopants

When introducing 3d transition metal elements, there are a few mechanisms that induce the observed valley splitting in our experiments. Firstly, it may be induced by a change in the local environments around the dopants. As we show in Figure S10, the atomic orbital character of the energy bands can partly be changed in the vicinity of dopants, altering the atomic orbital contribution to the valley splitting. To be specific, partial states in valence band in K valley turn from m_l = -2 to 0, and partial states of conduction band turn into m_l = -2, then the energy shift induced by this transition is

$$E_K^{im}(B) = \Delta^0 + (1-x)(2 - \Delta\alpha)\mu_B B + x[(-1 - \alpha_c - 2) + (1 + \alpha_v)]\mu_B B = E_K^0(B) - 4x\mu_B B, \quad (4)$$

where index "im" means the doping case, x is the Co dopant concentration. Therefore, we get

$$\Delta E_{im}(B) = E_K^{im}(B) - E_{-K}^{im}(B) = \Delta E_0(B) - 8x\mu_B B. \quad (5)$$

We define a relative ratio between the shift induced by local environment changes to the shift in pristine MoS_2 as $\gamma = 8x\mu_B B / \Delta E_0(B)$. In our experiment, at B=5 T, the valley splitting is 2.86 meV (x=0.8%), 3.54 meV (x=1.7%), and 4.22 meV (x=2.5%). For comparison, the valley splitting is 1.36 meV at B=5T for pristine MoS_2 in our experiment. Thus, the experimental data for γ are respectively 110% (doping 0.8%), 160% (doping 1.7%) and 210% (doping 2.5%). However, from eq. (5), the calculated γ for the local environment changes are 1.4% (0.8%),

2.894% (1.7%), and 4.26% (2.5%). We therefore conclude that the local change of energy bands induced by the dopants cannot afford the largely enhanced valley splitting.

Secondly, Magnetic impurities can modify the valley splitting by altering the effective masses of carriers in the K and -K valleys, which may be taken into account by

$$\Delta E_{\tau_z}^0(B) = \Delta\alpha^{\tau_z}\tau_z\mu_B B \qquad (6)$$

where $\tau_z = \pm 1$ for K and -K valley. When τ_z is at the locations of superscript or subscript, it only has the meaning of indicating the valleys. This term stems from the change of Berry curvature of each valley, *i.e.* the modification to the valley magnetic moment from a change in the effective mass. The effective mass of electrons and holes may now differ a) from each other (*i.e.* $m^*_c \neq m^*_v$) and b) from one valley to the other ($m^*_K \neq m^*_{-K}$).

Effective masses are more difficult to compute accurately in large supercells and are sensitive to the errors introduced by the exchange-correlation functional[9,13]. To determine the band contribution to the valley Zeeman splitting, we compute the effective mass of carriers via density functional theory (DFT) at the band edges about the valley minima (*i.e.* the band curvature about K along the Γ – K and K – M directions). The effective masses are identical for electrons and holes along Γ – K: m* is 1.09 m_0 at K and 0.59 m_0 at -K. Along K – M, the effective mass for electrons (holes) is 0.59 m_0 (1.17 m_0) at K and 0.66 m_0 (0.55 m_0) at -K. From **k·p** theory, $\alpha \simeq m_0/m^*$, so the difference between these effective masses gives a small additional slope of 0.03 meV/T. This value is quite small and we can safely ignore it.

2.3. Theory for enhanced valley splitting due to the internal magnetic field

Apart from the mechanism discussed above, we have to investigate the effect of the internal magnetic field B_{in} induced by the magnetic dopants. Single dopant and tri-dopant

configurations of impurities are identified. For single dopant, a Co atom replaces one Mo atom. There are 5 electrons with up spins occupying the 4d orbitals of one Mo atom; while 7 electrons on 3d orbitals of a Co atom, leaving 3 up spins occupying m_l = 2, 1, and 0, respectively. The electron with m_l = 2 takes part in bonding with the neighbor S atoms like what Mo atom plays. Comparing with Mo atom, there is no m_l = -2 state so that partial states at the valence band edge composing of m_l = -2 atomic orbital of Mo atoms will be missing, leaving some defects. Taking into account of these effects, we may conclude that the valley splitting induced by single dopants may not have a dramatic difference to that of pristine MoS_2, which at most means an induced valley splitting at the same order to that of pristine MoS_2 without enhancement.

Then, in the following, we show that the internal magnetic field formed by tri-dopants (dominant in our experiment) may explain the observed giant enhanced valley splitting. The essential ingredients are that the internal magnetic field interacts not only with the spin degree of freedom, but also with atomic orbital moments and the valley magnetic moments.

(1) We first establish the coupling between B_{in} and the carriers' spins at the locations of the local magnetic moments. The Hamiltonian is similar to the known s-d Hamiltonian $H_{ex} = \sum_n J(\boldsymbol{r} - \boldsymbol{R}_n)\, \boldsymbol{s} \cdot \boldsymbol{S}_n$, where n represent the locations of impurities, $\boldsymbol{s}$ and $\boldsymbol{S}_n$ are spin operators for itinerant carriers and the local magnetic impurities. Introducing the virtual crystal approximation[14] and the internal-magnetic-field approximation, we have

$$\begin{cases} H_{ex,\text{KC}} = x(N_0\beta)\langle S_z\rangle, \\ H_{ex,\text{KV}} = x(N_0\alpha)\langle S_z\rangle, \end{cases} \qquad (7)$$

where x is the density of dopants, "KC(KV)" means conduction (valence) band for K valley, $\alpha = \langle \text{KV}|J(\boldsymbol{r})|\text{KV}\rangle$, $\beta = \langle \text{KC}|J(\boldsymbol{r})|\text{KC}\rangle$, $|\text{KV(KC)}\rangle$ indicate the states for the valence (conduction) band in K valley, and $J(\boldsymbol{r}) = \sum_{\boldsymbol{R}} J(\boldsymbol{r} - \boldsymbol{R})$. Therefore, we have the energy shift for down spin in K valley as

$$\Delta E_{\mathrm{inter,K}} = H_{ex,\mathrm{KC}} - H_{ex,\mathrm{KV}} = -x(N_0\delta)\langle S_z\rangle, \quad (8)$$

Where "inter" means internal magnetic field case, $N_0\delta = N_0\beta - N_0\alpha$. For up spin in -K valley, $\Delta E_{\mathrm{inter},-\mathrm{K}} = -\Delta E_{\mathrm{inter,K}}$. Therefore, the valley splitting due to the coupling between spins and the internal magnetic field reads

$$\Delta E_{\mathrm{inter}}^{\mathrm{Spin}} = -2x(N_0\delta)\langle S_z\rangle, \quad (9)$$

which is distinct from the coupling between spin and the external magnetic field *B*, in which the coupling does not affect the PL position because the *B* couples equally to the conduction and valence bands. In the B_{in}-case, the spin-B_{in} coupling depends on the conduction and valence bands. Eq. (9) tells us clearly that the Zeeman coupling between spin does affect the PL position in our experiment. We can rewrite Eq. (9) as

$$\Delta E_{\mathrm{inter}}^{\mathrm{Spin}} = -2x\mu_B \frac{(N_0\delta)\langle S_z\rangle}{\mu_B}. \quad (10)$$

(2) In principle, there are 6 different exchange interaction strengths, i.e. J_{SC}, J_{SV}, J_{AC}, J_{AV}, J_{VC}, and J_{VV}. The meaning of J_{ij} is that i corresponds to one kind among spin (S), atomic (A), and valley magnetic moments (V); and j (=C, V) corresponds to conduction (C) band or valence (V) band. For example, J_{SC} describes the exchange interaction between the carrier's spin moment of conduction band and the internal magnetic field. When we include spin-, atomic orbital, and valley magnetic moment contributions, we get

$$\Delta E_{\mathrm{inter}} = 2\mu_B\langle S_z\rangle\left\{-x\frac{(N_0\delta)}{\mu_B} + 2x\frac{(N_0\langle J_{AV}\rangle)}{\mu_B} + x\left[-\frac{\alpha_C N_0\langle J_{VC}\rangle}{\mu_B} + \frac{\alpha_V N_0\langle J_{VV}\rangle}{\mu_B}\right]\right\}, \quad (11)$$

where $\langle J_{AV}\rangle = \langle KV|J_{AV}|KV\rangle$, $\langle J_{VC}\rangle = \langle KC|J_{VC}|KC\rangle$, $\langle J_{VV}\rangle = \langle KV|J_{VV}|KV\rangle$. Basically, these parameters can be determined by fitting the experimental data in terms of these formulas. To make a quick estimation, we would like to give a rough analysis. The simplest assumption is $N_0\delta = N_0\langle J_{AV}\rangle = N_0\langle J_{VC}\rangle = N_0\langle J_{VV}\rangle$. Thus, we get a simplified equation as

$$\Delta E_{\mathrm{inter}} = 2x(1-\Delta\alpha)\mu_B\langle S_z\rangle\left(\frac{(N_0\delta)}{\mu_B}\right) = 2x(1-\Delta\alpha)\mu_B B_{\mathrm{in}}, \quad (12)$$

where $B_{\mathrm{in}} = \langle S_z\rangle\left(\frac{(N_0\delta)}{\mu_B}\right)$.

Under the simplest assumption, the total energy shift measured by the shift of the PL peaks' positions is

$$\Delta E = \Delta E_0(B) + \Delta E_{\text{inter}} = 2(2 - \Delta\alpha)\mu_B B + 2x(1 - \Delta\alpha)\mu_B B_{\text{in}}. \qquad (13)$$

The internal magnetic field is expressed in terms of $\langle S_z \rangle$, which is given by the Brillouin function as

$$\langle S_z \rangle = -SB_S\left[\frac{gS\mu_B B}{k_B(T-T_0)}\right], \qquad (14)$$

where T_0 is positive and indicates a temperature reflecting the ferromagnetic coupling between the three Co dopant in a tri-dopant cluster, and

$$B_S(\xi) = \frac{2S+1}{2S}\coth\left[\frac{(2S+1)\xi}{2S}\right] - \frac{1}{2S}\coth\left(\frac{\xi}{2S}\right), \quad (15)$$

is the Brillouin function. We rewrite Eq. (13) as

$$\Delta E(B) = kB, \qquad (16)$$

where $k = 2(2 - \Delta\alpha)\mu_B + 2x(1 - \Delta\alpha)\mu_B\eta$, and $\eta = \frac{B_{\text{in}}}{B}$. In the following, we estimate the factors in the formalism by using the data at B=7 T. The experimental data are $x = 0.8\%, k = 0.56\ meV \cdot T^{-1} = 9.675\ \mu_B$; $x = 1.7\%, k = 0.72\ meV \cdot T^{-1} = 12.440\ \mu_B$; $x = 2.5\%, k = 0.87\ meV \cdot T^{-1} = 15.031\ \mu_B$. By using these data, we estimate $N_0\delta \approx -0.5$ eV, which is comparable to those found in dilute magnetic semiconductors[15]. We have to emphasize that a better value of various parameters can be determined by fitting the experimental data in terms of the full formula as

$$\Delta E = \Delta E_0(B) + \Delta E_{\text{inter}} = 2(2 - \Delta\alpha)\mu_B B + \Delta E_{\text{inter}}, \quad (17)$$

where ΔE_{inter} is given in Eq. (11).

Additional references:

[1] T. M. Masikhwa, F. Barzegar, J. K. Dangbegnon, A. Bello, M. J. Madito, D. Momodu, N. Manyala, *Rsc Adv* **2016**, 6, 38990.
[2] M. S. Faber, M. A. Lukowski, Q. Ding, N. S. Kaiser, S. Jin, *J Phys Chem C* **2014**, 118, 21347.
[3] Y. Ohno, *J Electron Spectrosc* **2008**, 165, 1.
[4] J. Klein, A. Kuc, A. Nolinder, M. Altzschner, J. Wierzbowski, F. Sigger, F. Kreupl, J. J. Finley, U. Wurstbauer, A. W. Holleitner, M. Kaniber, *2D Mater* 2017, 5, 011007.

[5] Y. M. He, G. Clark, J. R. Schaibley, Y. He, M. C. Chen, Y. J. Wei, X. Ding, Q. Zhang, W. Yao, X. D. Xu, C. Y. Lu, J. W. Pan, *Nat Nanotechnol* **2015**, 10, 497.
[6] A. Srivastava, M. Sidler, A. V. Allain, D. S. Lembke, A. Kis, A. Imamoglu, *Nat Nanotechnol* **2015**, 10, 491.
[7] G. Wang, L. Bouet, M. M. Glazov, T. Amand, E. L. Ivchenko, E. Palleau, X. Marie, B. Urbaszek, *2D Mater* **2015**, 2, 034002.
[8] A. Srivastava, M. Sidler, A. V. Allain, D. S. Lembke, A. Kis, A. Imamoglu, *Nat Phys* **2015**, 11, 141.
[9] G. Aivazian, Z. R. Gong, A. M. Jones, R. L. Chu, J. Yan, D. G. Mandrus, C. W. Zhang, D. Cobden, W. Yao, X. Xu, *Nat Phys* **2015**, 11, 148.
[10] J. Kim, X. P. Hong, C. H. Jin, S. F. Shi, C. Y. S. Chang, M. H. Chiu, L. J. Li, F. Wang, *Science* **2014**, 346, 1205.
[11] A. Arora, R. Schmidt, R. Schneider, M. R. Molas, I. Breslavetz, M. Potemski, R. Bratschitsch, *Nano Lett* **2016**, 16, 3624.
[12] F. Cadiz, E. Courtade, C. Robert, G. Wang, Y. Shen, H. Cai, T. Taniguchi, K. Watanabe, H. Carrere, D. Lagarde, M. Manca, T. Amand, P. Renucci, S. Tongay, X. Marie, B. Urbaszek, *Phys Rev X* **2017**, 7, 021026.
[13] H. J. Conley, B. Wang, J. I. Ziegler, R. F. Haglund, S. T. Pantelides, K. I. Bolotin, *Nano Lett* **2013**, 13, 3626.
[14] J. SINOVA, *Int J Mod Phys B* **2004**, 18, 1083.
[15] J. K. Furdyna, *J Appl Phys* **1988**, 64, R29.